Performance Evaluation of Type-II Superlattice Devices Relative to HgCdTe Photodiodes

M. Kopytko and A. Rogalski

***Abstract*—At present stage of infrared (IR) detector technology, two material systems, type-II superlattices (T2SLs) and HgCdTe ternary alloys, are used in fabrication of both mid- and long-wavelength IR arrays. The proposal of a new metric, the so-called "Law 19," motivates the estimation of the potential performance of HgCdTe photodiodes compared to that of T2SL photodetectors. In these circumstances, the evaluation for assessing the merit of HgCdTe detectors relative to novel III–V devices with respect to performance may change. This work attempts to estimate the change in the performance of HgCdTe photodiodes relative to T2SL detectors. The main comparative efforts concern such photodiode parameters as dark currents and noise equivalent temperature differences.**

***Index Terms*—HgCdTe, infrared (IR) detectors, Law 19, narrow bandgap semiconductors, Rule 07, type-II superlattices (T2SLs).**

I. INTRODUCTION

HITHERTO, there are two material systems used in fabrication of both mid-wavelength infrared (MWIR) and long-wavelength infrared (LWIR) focal plane arrays (FPAs): HgCdTe ternary alloys and III–V structures based on type-II superlattices (T2SLs). The position of the second class of materials has increased due to implementation of novel structures like barrier detectors, for example, nBn structures. Two years ago, Rogalski *et al.* have critically analyzed the performance of both class of photodetectors. From [1], results as follows.

- *III–V materials have inherently short Shockley–Read lifetimes below 1 μs and require nBn architecture to operate at reasonable temperatures and as such are diffusion current-limited. This applies both to the simple alloy and the T2SL versions.*
- *HgCdTe alloys have long Shockley–Read lifetimes >100 μs depending on the cut-off wavelength. They can thus operate with either architecture and may be diffusion or depletion current-limited.*
- *III–Vs offer similar performance to HgCdTe at an equivalent cut-off wavelength, but with a sizeable penalty in operating temperature, due to the inherent difference in Shockley–Read lifetimes.*

Important advantage of T2SLs is the high quality, high uniformity, and stable nature of the material. In general, III–V semiconductors are more robust than their II–VI counterparts due to stronger, less ionic chemical bonding. As a result, III-V-based FPAs excel in operability, spatial uniformity, temporal stability, scalability, producibility, and affordability—the so-called "ibility" advantages [2]. Moreover, the status of III–Vs materials can be strengthened since Hg-containing devices can potentially lead to health and environmental concerns.

At the current stage of HgCdTe technology development, the "Rule 07" metric (defined in 2007 [3]) is not an appropriate approach to predict the ultimate performance of the HgCdTe detector and system and as a benchmark for alternative infrared (IR) technologies. In 2019, Lee *et al.* [4] proposed replacing "Rule 07" with "Law 19" and presented a comparison of this fundamental limit with "Rule 07." In Kinch's well-known monograph [5], it was proved that the ultimate cost reduction of an IR system can only be achieved by using arrays operating at room temperature with a pixel density completely compatible with the background and diffraction-limited conditions of the system optics. After 60 years of HgCdTe history (its discovery was announced in 1959 [6]), this material system meets the above requirements and is still in a privileged position. To achieve this goal, a doping concentration in the active i-region (ν or π layer) of the p-i-n heterojunction photodiode below 5×10^{13} cm^{-3} is required. Such a low doping level and experimental data confirming theoretical predictions for fully depleted HgCdTe FPAs have been demonstrated by Teledyne Technologies [4], [7]. Under these circumstances, the assessment of the performance and cost advantages of HgCdTe detectors over III–V devices may change. The present work addresses this topic.

At the beginning, the evaluation of bulk HgCdTe and T2SL material systems is considered assuming a $\alpha\sqrt{\tau}$ value as a figure of merit, where α is the absorption coefficient and τ is the carrier lifetime. Then comparative studies of dark currents and noise equivalent difference temperature (NEDT) of photodetectors fabricated with bulk HgCdTe and two types

Manuscript received March 4, 2022; accepted March 26, 2022. Date of publication April 14, 2022; date of current version May 24, 2022. This work was supported in part by the National Science Centre (Poland) under Research Project 2018/30/M/ST7/00174 and in part by the National Centre for Research and Development (Poland) under Grant POIR.01.01.01-00-0185/20-00. The review of this article was arranged by Editor G. Ghione. *(Corresponding author: M. Kopytko.)*

The authors are with the Institute of Applied Physics, Military University of Technology, 00-908 Warsaw, Poland (e-mail: malgorzata.kopytko@wat.edu.pl; antoni.rogalski@wat.edu.pl).

Color versions of one or more figures in this article are available at https://doi.org/10.1109/TED.2022.3164373.

Digital Object Identifier 10.1109/TED.2022.3164373

This work is licensed under a Creative Commons Attribution 4.0 License. For more information, see https://creativecommons.org/licenses/by/4.0/

TABLE I
ESTIMATED FIGURE OF MERIT FOR THREE SETS OF MATERIAL SYSTEMS AT ROOM TEMPERATURE

Material system	Material parameters						
	Doping concentration	Absorption coefficient		Carrier lifetime		$\alpha\sqrt{\tau}$ [cm^{-1}s$^{1/2}$]	
		MWIR	LWIR	MWIR	LWIR	MWIR	LWIR
HgCdTe	5×10^{13} cm^{-3}	3.2×10^{3} cm^{-1}	2.2×10^{3} cm^{-1}	1 ms	0.1 ms	1.0×10^{2}	2.2×10^{1}
InAs/GaSb SLs	5×10^{14} cm^{-3}	2.4×10^{3} cm^{-1}	1.6×10^{3} cm^{-1}	20 ns	10 ns	3.4×10^{-1}	1.6×10^{-1}
InAs/InAsSb SLs	5×10^{14} cm^{-3}	1.2×10^{3} cm^{-1}	8.0×10^{2} cm^{-1}	25 μs	5 μs	2.4×10^{0}	3.6×10^{-1}

of type-II broken gap superlattices (SLs) (InAs/GaSb and InAs/InAsSb) are carried out.

II. DETECTOR MATERIALS FIGURE OF MERIT

The basic physical properties of bulk HgCdTe alloys are very well known and are described in many review papers and monographs, for example, in two monographs published in recent years [8], [9]. The InAs/GaSb SLs are better established than InAs/InAsSb ones. The former has been described in various review articles [10]–[12]. The latter emerged more recently with such advantages as simpler growth, better defect tolerance, and longer minority carrier lifetime [13], [14]. However, in comparison with InAs/GaSb SLs, the InAs/InAsSb SLs are characterized by smaller cut-off wavelength range, weaker optical absorption, and more challenging growth-direction (⊥) hole transport [14].

As is shown by Piotrowski and Rogalski [15], the performance of IR photodetectors is limited by the statistical nature of generation and recombination mechanisms in the semiconductor. It can be expressed by

$$D^* = \kappa \frac{\lambda}{hc}\left(\frac{\alpha}{G_{\text{th}}}\right)^{1/2} \quad (1)$$

where λ is the wavelength, h is the Planck constant, c is the speed of light, α is the absorption coefficient, and G_{th} (in cm^{-3}·s^{-1}) is the thermal generation in the active detector's region. κ is the coefficient dependent on radiation coupling of the detector including, for example, antireflection coating, microcavities, or plasmonic structures. α/G_{th} is the ratio of the absorption coefficient to the thermal generation rate. This ratio is the figure of merit of any IR detector material and can be utilized to predict the ultimate performance of any IR detector and to select materials that can be used as detector's active region.

The thermal generation rate G_{th} is defined as the rate at which a perturbed carrier system returns to equilibrium. For example, in a reversed-biased photodiode, it represents the rate at which carriers are generated within the diffusion length of the junction. As is shown by Kinch [5], the carrier generation rate can be expressed by

$$G_{\text{th}} = \frac{N_{\text{min}} t}{\tau} \quad (2)$$

where N_{min} is the minority carrier density, t is the detector thickness, and τ is the carrier lifetime. Since a typical detector thickness is $t = 1/\alpha$, where α is the absorption coefficient, then

$$G_{\text{th}} = \frac{N_{\text{min}}}{\alpha\tau}. \quad (3)$$

The thermal generation rate of minority carriers (e.g., holes in the n-type absorption region of the HgCdTe photodiode) is equal to

$$G_{\text{th}} = \frac{N_{\text{min}}}{\alpha\tau} = \frac{n_i^2}{\alpha N_{\text{maj}}\tau} \quad (4)$$

where N_{maj} is the majority carrier density and n_i is the intrinsic carrier concentration. In this case, the photodiode detectivity depends on

$$\propto D^*\left(\frac{\alpha}{G_{\text{th}}}\right)^{1/2} = \left(\frac{\alpha^2 N_{\text{maj}}\tau}{n_i^2}\right)^{1/2} = \left(\frac{\sqrt{N_{\text{maj}}}}{n_i}\right)\alpha\sqrt{\tau} \quad (5)$$

that is, the detectivity is proportional to the product of $\alpha\sqrt{\tau}$.

Recently, Kopytko and Rogalski have estimated $\alpha\sqrt{\tau}$ figure of merit [16] for three sets of material systems considered in this article and operated both in MWIR and LWIR regions. The absorption coefficients for HgCdTe ternary alloys are consistent with the empirical formula according to the article of Chu *et al.* [17]. For other materials, the threshold absorption coefficient is estimated for an energy of 1.2 E_g.

As can be seen from Table I, the $\alpha\sqrt{\tau}$ values for T2SLs are similar, but for HgCdTe is almost two orders of magnitude larger. This difference is mainly due to the much longer carrier lifetime in HgCdTe (in the microsecond range) with a lower doping concentration (below 5 × 10^{13} cm^{-3}) compared to their level in SL materials with doping 5 × 10^{14} cm^{-3}. In the case of InAs/GaSb T2SLs, the carrier lifetime is typically several tens of nanoseconds.

III. DARK CURRENT CONSIDERATION

Dark current density is an appropriate figure of merit which enables the comparison of potential performance of various IR photon detectors with different pixel sizes. It is more relevant than the zero-bias resistance–area product R_0A, which is not meaningful in T2SL barrier devices requiring a bias. For fully depleted HgCdTe photodiodes doped at 10^{13} cm^{-3} (for LWIR HgCdTe at 78 K, this doping is close to the intrinsic concentration n_i; at room temperature, the n_i value is three orders of magnitude larger), the scatter in the R_0A data can be large [18]. The efforts of many research groups to reduce dark current have focused on improving device design, material quality, and wafer processing.

Tennant *et al.* [3] have developed a simple empirical relationship that describes the dark current behavior with temperature and wavelengths for the better Teledyne HgCdTe diodes and arrays [primarily double-layer planar heterojunction (DLPH) structure devices]. It is called "Rule 07" and predicts the dark current density within a factor of 2.5 over a 13 order of magnitude range. It should be marked, however, that the "Rule 07" criterion is merely a manifestation of a detector architecture that is limited by Auger 1 diffusion currents from the 10^{15}/cm^3 n-type material. Any detector architecture that is limited by Auger 7 p-type diffusion or by depletion currents will not behave according to "Rule 07." Despite this, over time, "Rule 07" has become the reference benchmark for alternative technologies such as T2SLs, colloidal quantum dot, and 2-D material photodetectors.

In 2019, Lee *et al.* [4], [7] proposed replacing "Rule 07" with "Law 19" and provided a first attempt to compare both benchmarks. At present stage of technology, the fully depleted background limited HgCdTe photodiodes can reach the level of dark current considerably lower than predicted by the "Rule 07." The proposal of a new metric forces the ultimate properties of HgCdTe photodiodes.

In the present article, we have collected experimental dark current density values in T2SL photodetectors for their comparison with the new "Law 19" rule for HgCdTe [4], [7]. Values were obtained from texts, tables or graphs included in many publications. The considered cut-off wavelength range is from 4 to 14 μm, and it is divided into two ranges: MWIR range (4 to 5.5 μm) with a nominal operating temperature of 150 K [19]–[27] and LWIR range (8 to 14 μm) with a nominal operating temperature of 78 K [19], [28]–[41]. The cut-off wavelength was determined as the point of 50% response. In the presented figures, the experimental points are related to the research groups. Institution abbreviations and reference numbers are given in Table II.

The diffusion current arises from the thermal generation of carriers in the un-depleted semiconductor. Taking into account the radiative, Auger and Shockley–Read–Hall (SRH) mechanisms, the diffusion current density can be expressed as

$$J_{\mathrm{dif}} = \frac{q n_i^2 t_{\mathrm{dif}}}{N_{\mathrm{maj}}}\left(\frac{1}{\varphi \tau_R} + \frac{1}{\tau_A} + \frac{1}{\tau_{\mathrm{SRH}}}\right) \tag{6}$$

where q is the electron charge, t_{dif} is the diffusion region thickness, τ_R is the lifetime due to radiative recombination, φ is the product of the photon recycling factor for radiative recombination, τ_A is the lifetime due to Auger recombination, and τ_{SRH} is the lifetime for recombination through SRH centers in the bandgap.

The radiative process, in which an electron and a hole recombine to release energy by emitting a photon, is dominated in large-bandgap semiconductors. Due to the photon recycling effect [42], the radiative process is not considered to be a limiting factor for the IR device performance. Thus, the effective radiative lifetimes have been calculated using the van Roosbroeck and Shockley expression [43] multiplied by the photon recycling factor $\varphi = 10$ [44].

The Auger process involves three carriers (two majority carriers and one minority carrier) and becomes dominant at high temperatures and in heavily doped material. It depends sensitively on the semiconductor's electronic structure and can be limited by appropriate band structure engineering in T2SLs in order to remove possible final states in the Auger transition. The Auger lifetimes have been computed from the Landsberg theory [45]. The suppression of the Auger recombination rate in T2SL by a factor of about four relative to the bulk systems was observed [46], however, it appears that this suppression is largely due to the balancing the conduction and valence band masses rather than final-state structure. Another large uncertainty in the Landsberg model is the overlap integral F_1F_2 between electron wavefunctions.

The SRH mechanism, in which electron–hole (e–h) recombination is mediated by defects created mid-bandgap levels, is observed in a wide class of semiconductor compounds. Despite the SRH mechanism has been thoroughly investigated both theoretically and experimentally, beginning with pioneering work of Hall [47] and Shockley and Read [48], there are still some unresolved issues. The SRH rate depends primarily on the defect density N_T located at the energy level E_T below the conduction band edge of the semiconductor, and the recombination coefficients for electrons and holes (γ_n and γ_p), which are represented by the product of the capture cross sections of the relevant carrier and its thermal velocity. The shortest SRH lifetime occurs through defects located approximately at the intrinsic energy level in the semiconductor bandgap [5]. Then, at low temperatures, when $n > n_i$, we have $\tau_{\mathrm{SRH}} \approx \tau_{\mathrm{po}}$ in the n-type field-free region. At high temperatures, when $n \approx n_i$, we have $\tau_{\mathrm{SRH}} \approx \tau_{\mathrm{no}} + \tau_{\mathrm{po}}$, where $\tau_{\mathrm{no}} = (\gamma_n N_T)^{-1}$ and $\tau_{\mathrm{po}} = (\gamma_p N_T)^{-1}$.

When the SRH mechanism occurs within the depletion region, the carriers drift to their respective sides of the junction. Then the depletion current density [or generation-recombination (GR) current density] can be estimated by the following simple expression [5]:

$$J_{\mathrm{GR}} = \frac{q n_i W}{\tau_{\mathrm{SRH}}} \tag{7}$$

where W is the width of the depletion region. For the optimum E_T energy at the intrinsic energy level, we have $\tau_{\mathrm{SRH}} \approx \tau_{\mathrm{no}} + \tau_{\mathrm{po}}$. When the lifetimes of both carriers are identical ($\tau_{\mathrm{no}} = \tau_{\mathrm{po}} = \tau_{\mathrm{o}}$), $\tau_{\mathrm{SRH}} \approx 2\tau_{\mathrm{o}}$.

Since the SRH mechanism is not a fundamental limitation of semiconductor carrier lifetime, it might be overcome by a careful optimization of material technology or by using an appropriate detector architecture, for example, by inserting a wide-gap barrier near the junction region [49], [50].

When the effective carrier recombination lifetimes are sufficiently long, internal currents within the detector can be suppressed and the detector becomes limited by the background (bckg) radiation from the surrounding environment – background-limited infrared performance (BLIP) limit. The expression for the BLIP limit current density is

$$J_\phi = \eta q \Phi_B \tag{8}$$

where η is the quantum efficiency (QE), q is the electric charge, and Φ_B is the total background photon flux density reaching the detector

$$\Phi_B = \sin^2(\theta/2)\int_0^{\lambda_c} \frac{2\pi c}{\lambda^4\left[\exp(hc/\lambda k T_B) - 1\right]} \mathrm{d}\lambda \tag{9}$$

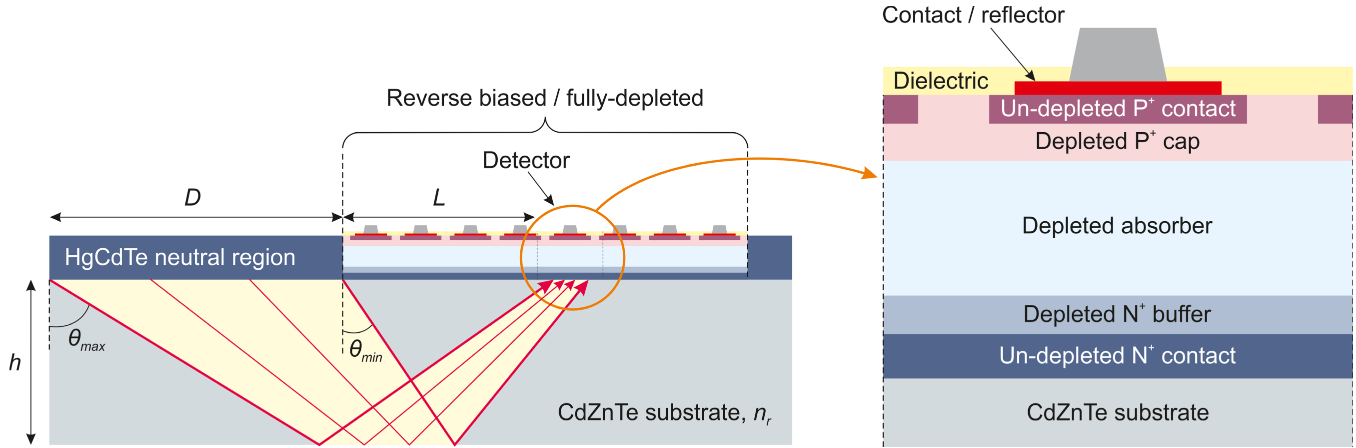

Fig. 1. Teledyne's heterojunction P-ν-N photodiode. Emission from neutral regions of the HgCdTe epilayer and subsequent reflection from the substrate–air interface increase the overall background radiation incident on a guarded detector. The amount of radiation captured by a detector depends on the distance of the edge of neutral region from the detector L, the extent of the neutral region D, and the substrate thickness h (adapted after [7]).

TABLE II
INSTITUTIONS REPORTING THE DARK CURRENT DENSITY VALUES COLLECTED FOR THIS STUDY

Institution	Abbreviation	References
Jet Propulsion Laboratory	JPL	19–22, 28–32
Naval Research Laboratory	NRL	33,34
SemiConductor Devices	SCD	35
Raytheon Vision Systems	RVS	36–38
i3system Inc.	i3system	23
IRnova AB	IRnova	24
Electronic Institute of the University of Montpellier/CRNS	IES/CRNS	25
Northwestern University	NWU	26,27
University of New Mexico	UNM	39,40
Arizona State University	ASU	41
Teledyne Imaging Sensors	Teledyne	4,7

where θ is the cone angle, c is the light velocity, λ_c is the detector cut-off wavelength, k is the Boltzmann constant, and T_B is the background temperature. Assuming an ideal unity QE, Eq. (8) leads to the analytical expression for "Law 19" [7]

$$J_{\text{rad}} = qC_1\left(a^2 + 2a + 2\right)\exp(-a) \tag{10}$$

where

$$C_1 = 1.7\times10^{18}(T/300)^3 \tag{11}$$

$$a = 48 \times (300/\lambda_c T) \tag{12}$$

and T is the detector's temperature.

It should be noted that the high refractive index n_r of the CdZnTe substrate can have a significant effect on the overall background radiation incident on the P-ν-N detector (see Fig. 1) [7]. Under reverse bias, the ν-absorber and part of the wide bandgap P- and N-regions are depleted. Any carriers are swept to the junction in a time that is short compared to the radiative lifetime, so the detector itself does not radiate significantly. However, the un-depleted neutral regions of the HgCdTe epilayer radiate with a blackbody spectrum for energies exceeding the absorber bandgap. Most of this radiation is completely reflected internally at the substrate-air interface and can be captured by the detector. Consequently,

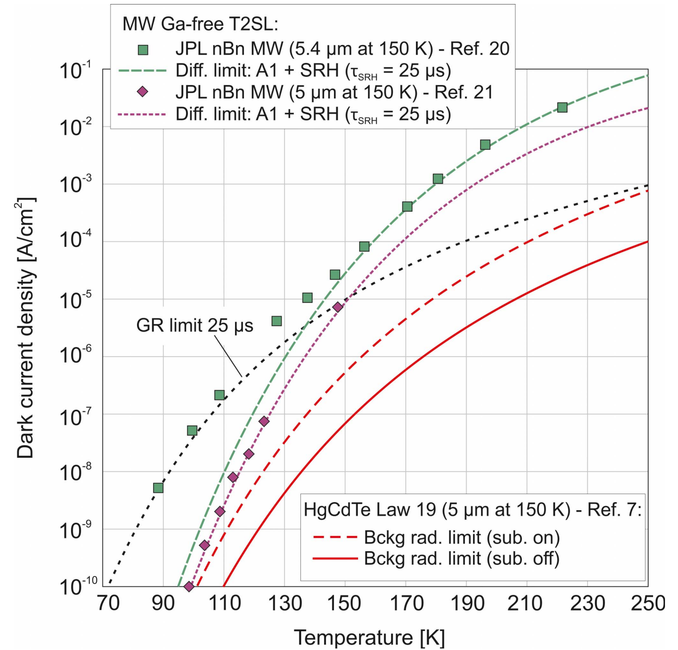

Fig. 2. Temperature dependence of dark current density of MWIR T2SL nBn detectors. The experimental data have been taken from [20] and [21]. Background radiation limit has been calculated for the HgCdTe absorber [7] with the change in energy gap with a temperature typical for HgCdTe.

the incident radiation is increased by n_r^2, that is, the so-called "substrate-on" radiation limit is increased by approximately 7.3 factor, compared to the value described by (10), which is defined as a "substrate-off" radiation limit.

We have calculated the temperature-dependent dark current densities of representative T2SL and HgCdTe absorber layers, assuming that the saturation current is the sum of the diffusion and depletion current. Specific parameters used in the calculations are listed in Table III. Other relations used in device modeling are given in the Appendix.

IV. DARK CURRENT CHARACTERISTICS—STATE OF THE ART

Fig. 2 shows the temperature dependence of dark current densities of InAs/InAsSb T2SL nBn detectors fabricated by

TABLE III
MATERIAL PARAMETERS OF ACTIVE LAYERS

Absorber parameter	Detector type				
	nBn	**nBn**	**n-CBIRD**	**p-CBIRD**	**P-ν-N**
Material	InAs/InAsSb	InAs/InAsSb	InAs/InAsSb	InAs/GaSb	HgCdTe
Cut-off wavelength, λ_c [μm]	5.37 (150 K)	4.98 (150 K)	10.1 (77 K)	9.9 (77 K)	10.2 (78 K)
Bias, U [V]	-0.2	-0.1	-0.15	-0.2	-0.25
Doping, $N_{D,A}$ [cm^{-3}]	1×10^{15}	5×10^{14}	1×10^{15}	1×10^{16}	1×10^{13}
Thickness, t_{abs} [μm]	2.6	3.9	3.4	3.9	3
Electron effective mass, m_e^*/m_0	0.022	0.022	0.021	0.0183	$0.071\times E_g$
Hole effective mass, m_{hh}^*/m_0	0.21	0.17	2.06	0.122	0.55
SRH carrier lifetime, τ_{SRH} [ms]	0.025	0.025	5×10^{-3}	2×10^{-3}	0.5
Overlap matrix F_1F_2	0.2	0.2	0.05	0.2	0.2

Jet Propulsion Laboratory (JPL) [20], [21] with a cut-off wavelength of 5 μm at 150 K. The experimental data have been compared to the background radiation limit, which has been calculated for an HgCdTe absorber with a bandgap corresponding to the cut-off wavelength of 5 μm at 150 K and assuming a change in the energy gap with a temperature typical for HgCdTe, according to Hansen *et al.* [51]. Earlier, nB_pn (p-type barrier) InAs/InAsSb detection structure presented by JPL in [20] (green squares) indicates diffusion-limited dark current behavior at high temperature range (157–222 K). The presence of GR dark current, due to a p-n junction located at the p-type barrier and n-type absorber interface, is apparent at temperatures below 128 K, with a fitted SRH lifetime of $\tau_{SRH} = 25$ μs. Dark currents of a modified nB_nn (n-type barrier) InAs/InAsSb detector [21] (purple diamonds) are well approximated by the expression for the diffusion current in the whole reported temperature range (99–148 K). The absence of observable GR current is the result of the lack of a depleted region due to the homogeneous n-type doping through the entire heterostructure. The dark current density is $\sim 5 \times 10^{-6}$ A/cm^2 at 150 K and is the lowest dark current density for InAs/InAsSb MWIR detector reported so far. However, this value is 14× that of HgCdTe "substrate-on" radiative limit and 100× "substrate-off" radiative limit ("Law 19"). At 99 K, the dark current density of InAs/InAsSb detector decreases to 1×10^{-10} A/cm^2 and achieves the value for the HgCdTe "substrate-on" radiative limit. However, it should be noted that the HgCdTe energy gap changes in an opposite way with temperature than the T2SL energy gap.

The collected dark current density data at 150 K as a function of device cut-off in the MWIR, with "Rule 07" and "Law 19" curves for comparison, are shown in Fig. 3. So far, the lowest dark current densities for Ga-free MWIR T2SL photodetectors have been reported by JPL (purple open diamonds), with values 2.5× higher than "Rule 07." These data have been collected from papers of the last three years, showing that T2SL photodetectors are approaching the performance of HgCdTe photodiodes. In the meantime, however, "Rule 07" has been replaced by "Law 19." The introduction of fully depleted HgCdTe P-ν-N photodiodes demonstrated by Teledyne Technologies [7] has set a new trend in ultimate performance, which will be particularly difficult to achieve for T2SL photodetectors in the LWIR range.

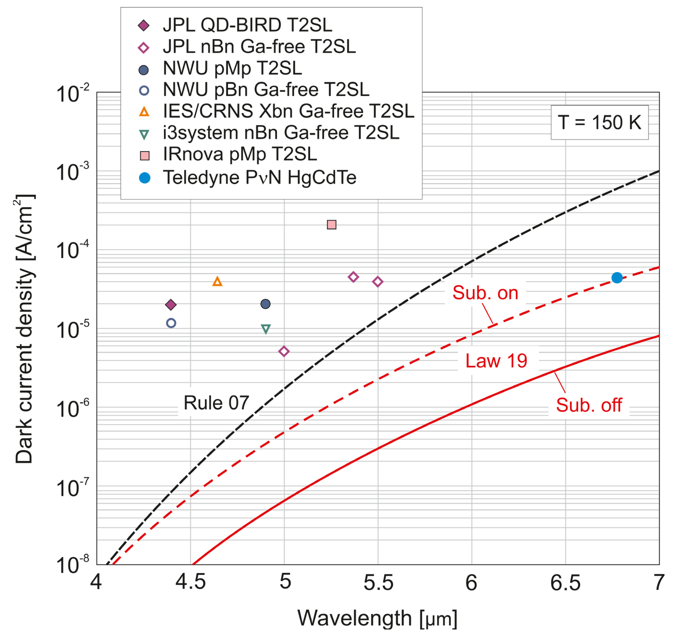

Fig. 3. Results of the survey of published dark current density data in MWIR T2SL photodetectors at 150 K, with HgCdTe "Rule 07" and "Law 19" for comparison. The experimental data have been taken from different sources collected in Table II.

Temperature dependence of the dark current density of the LWIR InAs/GaSb T2SL [30], InAs/InAsSb T2SL [32], and HgCdTe [7] detectors is presented in Fig. 4. The excess current at 78 K (and below) is GR-limited, assuming an SRH lifetime of 5 μs for InAs/InAsSb T2SL, 2 μs for InAs/GaSb T2SL, and 0.5 ms for HgCdTe. The dark current density of the T2SL device is $\sim 4 \times 10^{-5}$ A/cm^2 at 78 K and is 30× higher than that of the HgCdTe one. In the high-temperature range, the T2SL detector (dark blue squares) is diffusion-limited with dark currents two orders of magnitude larger than the HgCdTe detector (red open circles) showing the "substrate-on" radiative limit. Furthermore, the T2SL detector is characterized by a much lower QE - peak QE at the level of 25%, whereas the peak QE of the HgCdTe detector is nominally at the theoretical limit (see Fig. 5).

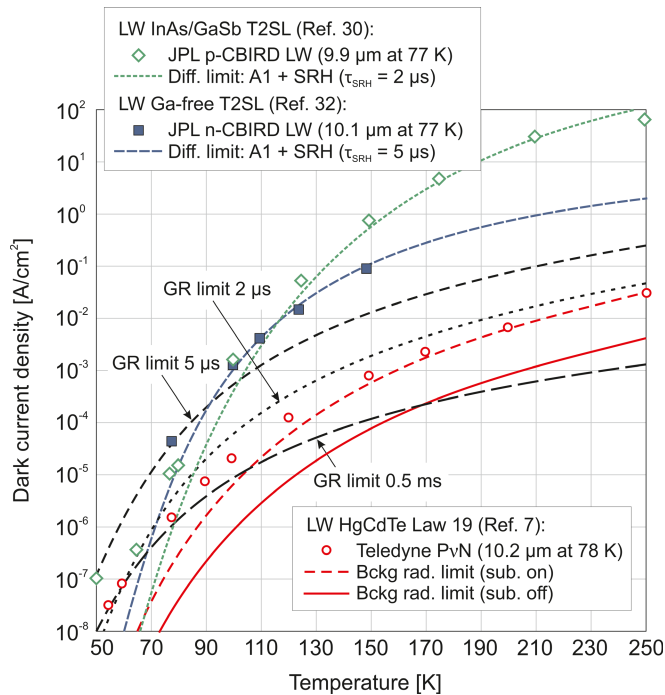

Fig. 4. Temperature dependence of dark current density of LWIR T2SL n-CBIRD and P-ν-N HgCdTe detectors. The experimental data have been taken from [7], [30], and [32]. Background radiation limit has been calculated for the HgCdTe absorber with the change in energy gap with a temperature typical for HgCdTe.

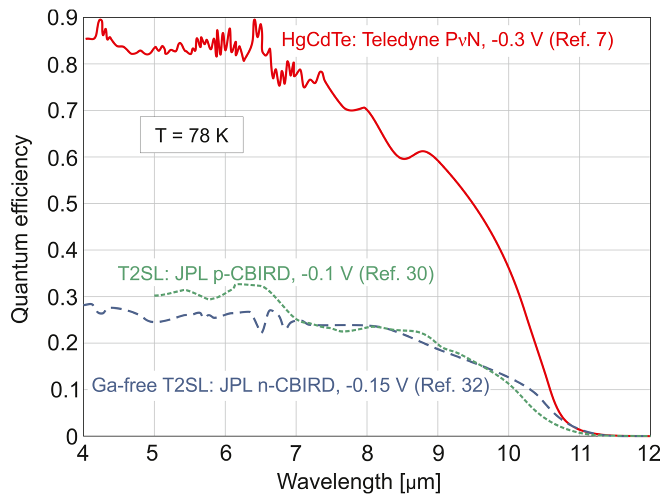

Fig. 5. Spectral QE for LWIR Ga-free T2SL n-CBIRD, T2SL p-CBIRD, and P-ν-N HgCdTe detectors at 78 K. The experimental data have been taken from [7], [30], and [33]. The QE of T2SL device has not been corrected for substrate reflection or transmission (~one-third of the incident light is reflected by the GaSb substrate).

The main technological challenge for the fabrication of T2SL detectors is the growth of thick active layers without degrading the materials quality. High-quality SL materials thick enough to achieve acceptable QE is crucial to the success of the technology. For T2SL photodiodes with typical active area thicknesses between 3 and 4 μm, the QE is 30%–40%. More information on this subject can be found, for example, in the monograph [12] and the recently published paper [16].

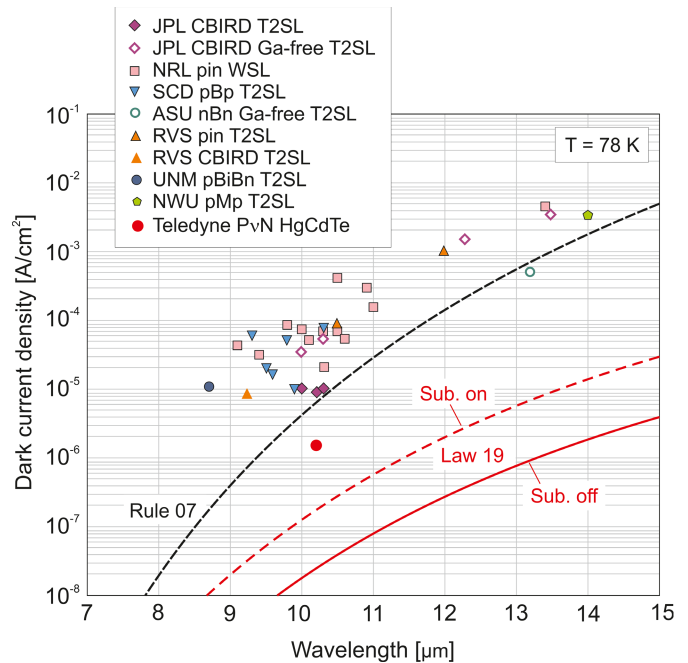

Fig. 6. Results of the survey of published dark current density data in LWIR T2SL detectors at 78 K, with HgCdTe "Rule 07" and "Law 19" for comparison. The experimental data have been taken from different sources collected in Table II.

Fig. 6 shows a plot of a collected dark current density data at 78 K as a function of device cut-off in the LWIR range, with the "Rule 07" and "Law 19" curves for comparison. In this case, the dark current density of T2SL devices close to the "Rule 07" line is reported for a cut-off wavelength of $\geq$10 μm. The GR process due to the SRH mechanism in the depleted absorber is the dominant source of current in the HgCdTe P-ν-N photodiode at 78 K. The advantages of a device operating with the use of a fully-depleted absorber are revealed at higher temperatures. As presented in Fig. 4, the HgCdTe photodiode exhibits radiatively limited ("substrate-on" limit) behavior at and above approximately 160 K. For T2SL devices to approach this limit, their dark currents should be reduced by two orders of magnitude.

Comparison of detector parameters over a wide range of wavelengths is possible when we plot the dark current density as a function of normalized E_g/kT product, where E_g is the semiconductor energy gap. In Fig. 7, the data of the best T2SL detectors in the MWIR and LWIR ranges have been compared with the latest Teledyne data for HgCdTe photodiodes.

A relatively short SRH lifetime in T2SLs, several orders shorter than that in HgCdTe, forces the use of the nBn architecture with no depletion region. The dark currents of MWIR T2SL detectors follow a diffusion trend line, even at low temperatures—see the data reported at 2019 by JPL (purple diamonds). A homogeneous n-type doping along the entire heterostructure causes the absence of observable GR current. The detector is purely diffusion-limited, the main limiting factor is the background doping, and the lowest reported in T2SLs is in the mid 10^{14} cm^{-3} [21] (typically around 10^{15}–10^{16} cm^{-3}).

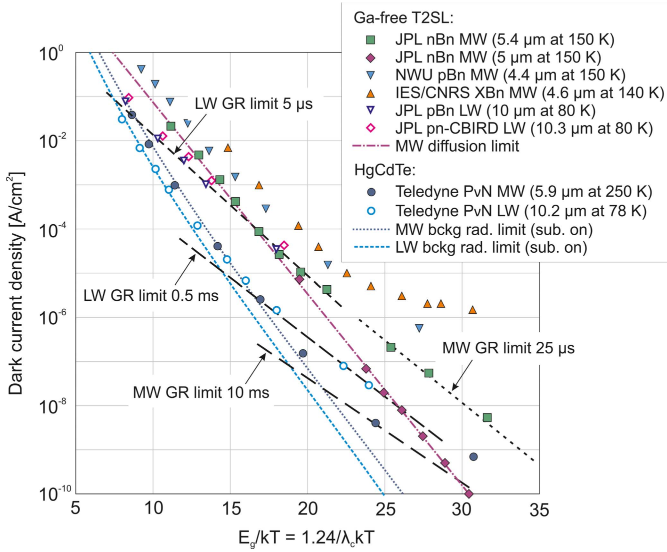

Fig. 7. Dark current as a function of normalized E_g/kT product in HgCdTe and T2SL development. The experimental data have been taken from different sources collected in Table II.

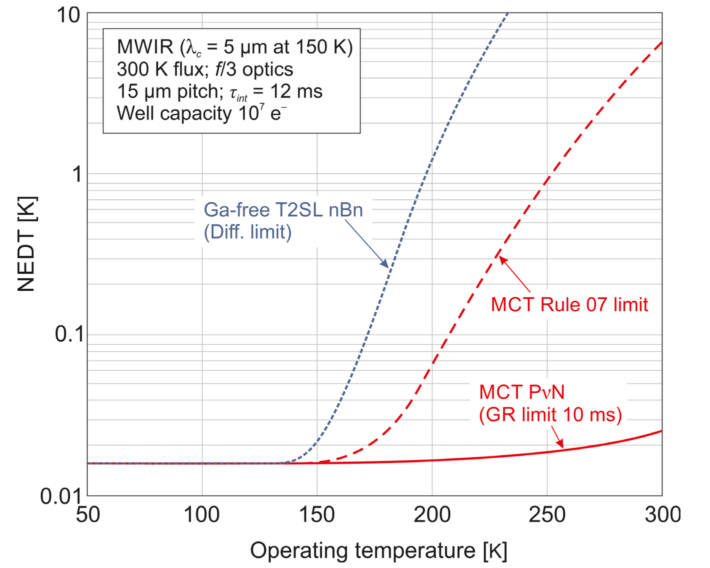

Fig. 8. Predicted temperature dependence of the NEDT for the MWIR Ga-free T2SL nBn detector and HgCdTe P-ν-N photodiode with comparison to the “Rule 07” limit.

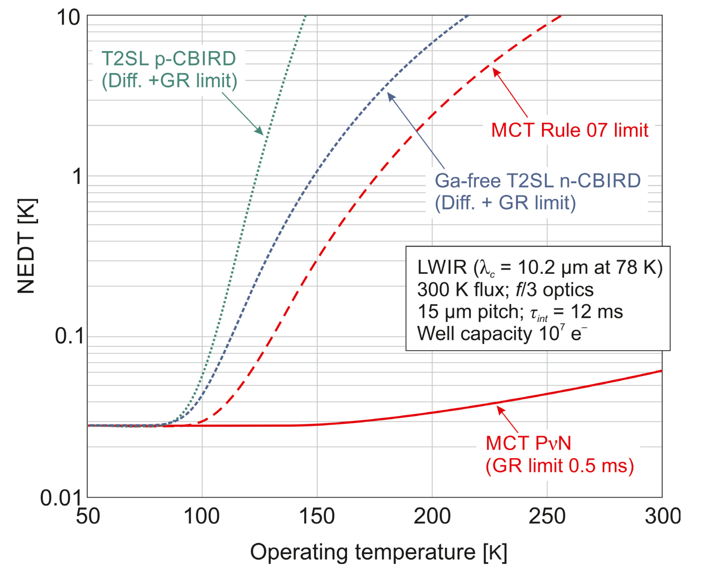

Fig. 9. Predicted temperature dependence of the NEDT for LWIR Ga-free T2SL n-CBIRD, T2SL p-CBIRD, and HgCdTe P-ν-N photodiode with comparison to the “Rule 07” limit.

More problematic is the LWIR range, where to avoid an excessively large growth-direction hole conductivity effective mass, p-type doping or a relatively high Sb fraction InAsSb in the absorber T2SL is used in a complementary barrier IR detector (CBIRD). Since the p-type doping entails many complications, for example, passivation is required to protect the etched slope of the detector mesas (the surface of the InAs/InAsSb T2SL is degenerate n-type, even when it is p-doped), the latter solution is more desirable. In addition, a graded-gap SL in the n-type absorber is proposed to provide a built-in field to assist the hole transport [30]. The above-mentioned problems of T2SLs mean that in the LWIR range, this material will not be competitive for HgCdTe. The progress made by Teledyne, which has reduced the background HgCdTe doping to 10^{13} cm^{-3} and long SRH lifetimes (10 ms at MWIR and 0.5 ms at LWIR) has allowed the development of fully-depleted photodiodes that are radiation-limited at high temperatures.

V. Noise Equivalent Difference Temperature

The FPA sensitivity can be expressed by the NEDT. This parameter is a figure of merit of thermal imagers. NEDT can be determined when the detector dark current density J_d and the background flux current density J_φ are known [5]

$$\mathrm{NEDT} = \frac{1+J_d/J_\phi}{\sqrt{N}C} \tag{13}$$

where

$$C = (\mathrm{d}\Phi_B/\mathrm{d}T)/\Phi_B$$

is the scene contrast through the optics.

The well capacity N available for normal scene integration must be at least equals to

$$N = \frac{(J_d + J_\phi)A\tau_{\mathrm{int}}}{q} \tag{14}$$

where A is the detector area, τ_{int} is the maximum available integration time, and q is the elementary charge. Values for N are typically in the range of 10^6–10^8 electrons for a 15-μm pixel design with available node capacitances for current CMOS readout integrated circuit designs. Keeping in mind the dark current considerations of Section IV, we can now model their impact on the NEDT performance for FPA. For comparison purposes, we will limit our considerations to an available integration time of 12 ms and a maximum usable well capacity of 10^7 electrons.

Figs. 8 and 9 show the temperature dependence of NEDT for FPAs based on T2SL barrier detectors and a fully-depleted P-ν-N HgCdTe photodiode designed for the MWIR and LWIR

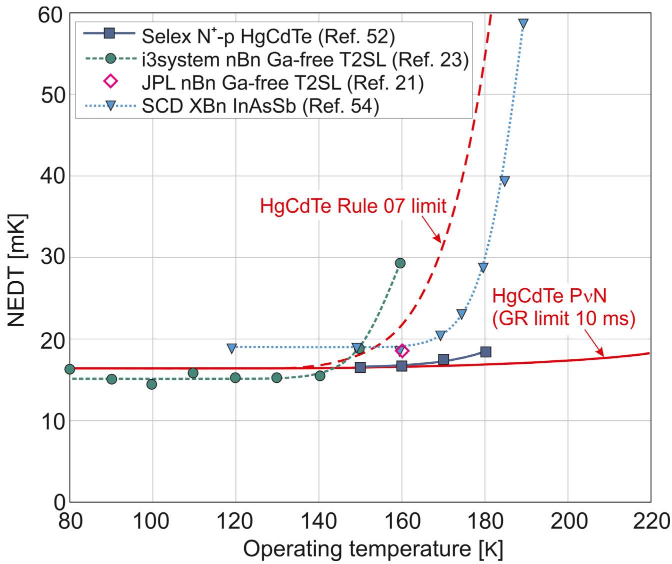

Fig. 10. Temperature dependence of the NEDT for MWIR Ga-free T2SL, InAsSb, and HgCdTe FPAs. The experimental data have been taken from Refs [21], [23], [52] and [54].

ranges, respectively. We have assumed that T2SL barrier detectors operate in the diffusion-limited condition, while the HgCdTe P-ν-N photodiode operates in the GR-limited condition—the depletion region occupies the entire absorption volume. Moreover, the diffusion-limited condition of HgCdTe photodiodes, estimated by "Rule 07," has been taken into account. In the low-temperature range, the NEDT of both material systems provide similar performance: 16 mK for MWIR and 30 mK for LWIR range, as they are limited by the well size and readout. For the temperature higher than 140 K for the MWIR and 80 K for the LWIR, the NEDT increases proportional to the dark current. Then, the theoretical performance limit of HgCdTe photodiode is more favorable than T2SL barrier detectors. The higher diffusion current component dominant in T2SL detectors significantly degrades the NEDT performance. The modeled GR-current component of P-ν-N HgCdTe photodiodes with SRH carrier lifetimes of 10 and 0.5 ms in the MWIR and LWIR, respectively, has a little effect on the NEDT at near room temperature with respect to the other types of detectors considered in this article (both SL devices and p-on-n HgCdTe photodiodes estimated by "Rule 07").

Fig. 10 shows the experimental NEDT values for MWIR FPAs that can be found in the literature. For HgCdTe technology, we have chosen the best quality arrays—Hawk detectors with 640 × 512 pixels, 16-μm pitch, and the cut-off wavelength of 5.2 μm at 150 K (SELEX Galileo Infrared Ltd.) [52]. The reported temperature dependence of NEDT is impressive, with a value of 18 mK at 180 K, also pointed out by Kinch [5]. These experimental data are close to the GR limit rather than the diffusion limit ("Rule 07" dark current limit), both calculated for a 300 K background flux current for $f/4$ optics and QE of 80%. The lowest reported dark current density at 180 K for this FPA is $\sim 4 \times 10^{-6}$ A/cm^2 and lies two orders of magnitude below the "Rule 07" limit, consistent with the longer lifetimes predicted for Auger 7 for the Hawk fabricated N$^+$-p HgCdTe photodiode with a 3-μm thick As-doped ($N_A = 10^{15}$ cm^{-3}) p-type absorber. Martyniuk *et al.* [53] explained this by possible photon recycling or suppression of band-to-band transitions through very fast capture of excess minority carriers (electrons) by an "empty" set of donor defects.

The experimental data of the NEDT for the 640 × 512 pixels Ga-free T2SL array with 15-μm pitch nBn detectors with the cut-off wavelength of 4.9 μm at 150 K (i3system Inc.) shows a constant value of 15 mK below 150 K (green circles). The NEDT has been measured with the 20° background flux current with $f/4$ optics [23]. At higher temperatures, the NEDT strongly increases in proportion to the dark current. At 160 K, the NEDT value is much higher than that reported by JPL for the 640 × 512 pixels Ga-free T2SL array with 24-μm pitch nBn detectors [21]: the measured NEDT for the 300 K background flux current with $f/2$ optics is 18.7 mK (pink open diamond). Fig. 10 also shows the NEDT for a typical InAsSb 15-μm pitch XBn Pelican-D FPA, measured with an aperture of $f/3.2$ in front of a blackbody at a temperature of 50 °C (blue inverted triangles) fabricated by SemiConductor Devices [54]. The dark current strongly affects performance above 160 K.

VI. Conclusion

The predicted "Law 19" for HgCdTe photodiode performance established in 2019 [4] is a milestone in the development of IR photodetectors and make the dream of Elliott and colleagues, who in 1999 wrote *that there is no fundamental obstacle to obtaining room-temperature operation of photon detectors at room temperature with background-limited performance even in reduced fields of view* [55]. In this situation, the "Law 19" forces the verification of the advantages of the HgCdTe material system over the novel III–V materials (type-II broken-gap SLs), with respect to their suitability as the active region of an IR photodetector.

After 60 years of HgCdTe technology development, Teledyne Technologies demonstrated the doping concentration in the active ν-region of a P-ν-N heterojunction photodiode below 5×10^{13} cm^{-3} and long SRH lifetimes above 100 μs [4], [7]. This experimental fact strengthens the position of HgCdTe as a still preferred material for the fabrication of high-operating-temperature (HOT) photodetectors. III–V materials have inherently short SRH lifetimes and require a barrier architecture to operate at reasonable temperatures.

At reverse bias voltage typically about 1–2 V, the free electrons in the active i-region are removed, and the dark current limited by Auger 1 recombination mechanism is suppressed to the level dominated by the background seen by the detector. In this way, the current dominated by background is by a factor of 10–100 lower than predicted by "Rule 07" depending on the cut-off wavelength and operating temperature. The advantage of P-ν-N HgCdTe photodiodes using a fully depleted absorber compared to T2SL devices is revealed especially at higher temperatures as indicated by significantly lower dark current densities and acceptable NEDT values.

TABLE IV
MATERIAL PARAMETERS OF InAs/InAsSb T2SL

Parameter	Detector type			
	nBn	**nBn**	**n-CBIRD**	**p-CBIRD**
T2SL	InAs/InAsSb	InAs/InAsSb	InAs/InAsSb	InAs/GaSb
Cut-off wavelength, λ_c [µm]	5.37 (150 K)	4.98 (150 K)	10.1 (77 K)	9.9 (77 K)
Bandgap at 0 K, E_{g0} [eV]	0.254	0.275	0.135	0.139
A [eV/K]	2.4×10^{-4}	3×10^{-4}	4×10^{-4}	4×10^{-4}
B [K]	85.85	95	95	95
Horizontal electron effective mass, $m^*_{e\parallel}/m_0$	0.02	0.02	0.018	0.018
Vertical electron effective mass, $m^*_{e\perp}/m_0$	0.0275	0.0275	0.028	0.019
Horizontal hole effective mass, $m^*_{hh\parallel}/m_0$	0.04	0.04	0.05	0.035
Vertical hole effective mass, $m^*_{hh\perp}/m_0$	6	3	3500	1.49

Recently demonstrated fully depleted 640 $\times$ 512 arrays (in MWIR and LWIR operated up to 250 and 160 K, respectively [7], [56]) gave a unique capability to produce the largest format arrays. It is expected that further technological improvement of depleted P-ν-N HgCdTe photodiodes with lower doping level in the active region (about 10^{13} cm^{-3} [7]) will increase the operating temperature of both MWIR and LWIR photodiodes close to 300 K. MWIR room-temperature HgCdTe photodiode arrays are expected to be produced soon (in a few years), while long-LWIR arrays are expected to be produced in the longer term.

However, it should be noted that several aspects important for the development of semiconductor materials technology are not considered in this article. For example, T2SLs are the III–V materials with a much larger industrial base to produce devices at a low cost in comparison with HgCdTe (HgCdTe as the II–VI material covers only IR detector market and has no other commercial leveraging) [1]. Moreover, in general, III–V semiconductors are more robust and stable than their II–VI counterparts due to stronger, less ionic chemical bonding. The growth of T2SLs can be carried with better control over the structure and grater reproducibility. Consequently, these materials are relatively easy to process, offering a cost-effective advantage over HgCdTe detectors. As a result, the 3-Mpixel FPA's resolution at 5-μm has been produced using advanced processing techniques that include high aspect ratio dry etching for mesa delineation that maintains a high fill factor, an optimal indium bump layout, and maximized array connectivity. III–V-based FPAs excel in operability, spatial uniformity, temporal stability, scalability, producibility, and affordability—the so-called "ibility" advantages [14]. For these reasons, III–V barrier detectors will be developed in the future, even though the fundamental physical properties better predispose HgCdTe ternary alloys to HOT operation.

III–V materials offer similar performance to HgCdTe at an equivalent cut-off wavelength, but with a sizeable penalty in the operating temperature, due to the inherent difference in SRH lifetimes [1], [57]. However, the ultimate cost reduction for an IR system will only be achieved by the room-temperature operation of arrays with pixel densities that are fully consistent with background and diffraction-limited performance due to the system optics [5]. The physical properties of HgCdTe situate this material system closer to achieving this goal. Also, HgCdTe technological challenges and problems conditioned by weaker crystalline bonds will be more efficiently overcome under HOT conditions of photodetector operation.

APPENDIX

The HgCdTe energy gap has been calculated according to the empirical relation given by Hansen *et al.* [51]

$$E_g(x,T) = -0.302 + 1.93x - 0.81x^2 + 0.832x^3 + +5.35\times10^{-4}(1-2x)T \quad \text{(A1)}$$

where E_g is in [eV], T is the temperature in [K], and x is the Cd molar composition.

The intrinsic carrier concentration n_i in HgCdTe has been calculated using the most widely used expression of Hansen and Schmit [58]

$$n_i = (5.585 - 3.82x + 0.001753T + 0.001364xT) \times 10^{14} E_g^{3/4} T^{3/2} \exp\left(-\frac{E_g}{2kT}\right) \quad \text{(A2)}$$

where k is the Boltzmann constant in [eV/K].

The effective masses m_e of electrons in the narrow-gap HgCdTe can be approximated by $m_e^*/m_0 = 0.071E_g$, while the effective mass of heavy holes according to $m_{hh}^*/m_0 = 0.55$, where m_0 is the free electron mass.

The T2SL energy gap has been calculated taking into account the cut-off wavelength temperature dependence and fitting to the Varshni expression [59]

$$E_g(T) = E_{g0} - \frac{AT^2}{(B+T)} \quad \text{(A3)}$$

where E_{g0} is the bandgap at 0 K and A and B are fitting parameters characteristic of a given material. Table IV shows the values of the appropriate parameters for analyzed detectors.

T2SL intrinsic carrier concentration was calculated according to the parabolic energy band approximation from the following relation:

$$n_i = 2\left(\frac{2\pi k}{h^2}\right)^{3/2}\left(m_e^* m_{hh}^*\right)^{3/4} T^{3/2} \exp\left(-\frac{E_g}{2kT}\right) \quad \text{(A4)}$$

where h is the Planck constant.

Effective masses for T2SLs were calculated according to

$$m_{e,hh}^* = \left[\left(m_{e,hh\parallel}^*\right)^2 m_{e,hh\perp}^*\right]^{1/3} \quad \text{(A5)}$$

where $m_{e,hh\parallel}^*$ and $m_{e,hh\perp}^*$ are in-plane and growth direction effective masses, respectively. A major concern for T2SL absorbers is the electron and hole effective masses [60], [61]. The lowest conduction subband ($C1$) band shows strong dispersion along both the growth ($\perp$; vertical) and in-plane ($\parallel$; horizontal) directions. The highest valence subband (HH1) also shows strong dispersion in the in-plane direction but appears nearly dispersionless along the growth direction. The HH1 zone-center effective mass along the growth direction for 10 μm cut-off absorber is $m_{hh\perp}^* = 3500 m_0$, which is almost five orders of magnitude larger than the electron effective mass: $m_{e\perp}^* = 0.015 m_0$. It should be noticed that the valence band mixing significantly decreases $m_{hh\perp}^*$ value away from the zone center [62], [63]. All values of effective masses adopted for the calculation of dark currents of the analyzed detectors are given in Table IV.

References

[1] A. Rogalski, P. Martyniuk, and M. Kopytko, "Type-II superlattice photodetectors versus HgCdTe photodiodes," *Prog. Quantum Electron.*, vol. 68, Nov. 2019, Art. no. 100228, doi: 10.1016/j.pquantelec.2019.100228.

[2] P.-Y. Delaunay, B. Z. Nosho, A. R. Gurga, S. Terterian, and R. D. Rajavel, "Advances in III-V based dual-band MWIR/LWIR FPAs at HRL," *Proc. SPIE*, vol. 10177, May 2017, Art. no. 101770T, doi: 10.1117/12.2266278.

[3] W. E. Tennant, D. Lee, M. Zandian, E. Piquette, and M. Carmody, "MBE HgCdTe technology: A very general solution to IR detection, described by 'rule 07,' a very convenient heuristic," *J. Electron. Mater.*, vol. 37, no. 9, pp. 1406–1410, Sep. 2008, doi: 10.1007/s11664-008-0426-3.

[4] D. Lee *et al.*, "Law 19—The ultimate photodiode performance metric," *Proc. SPIE*, vol. 11407, May 2020, Art. no. 114070X.

[5] M. A. Kinch, *State-of-the-Art Infrared Detector Technology*. Bellingham, WA, USA: SPIE, 2014, doi: 10.1117/3.2072367.

[6] W. D. Lawson, S. Nielsen, E. H. Putley, and A. S. Young, "Preparation and properties of HgTe and mixed crystals of HgTe-CdTe," *J. Phys. Chem. Solids*, vol. 9, nos. 3–4, pp. 325–329, Mar. 1959, doi: 10.1016/0022-3697(59)90110-6.

[7] D. L. Lee *et al.*, "Law 19: The ultimate photodiode performance metric," *Proc. SPIE*, vol. 11407, May 2020, Art. no. 114070X, doi: 10.1117/12.2564902.

[8] P. Capper and J. Garland, Eds., *Mercury Cadmium Telluride*. Hoboken, NJ, USA: Wiley, 2010, doi: 10.1002/9780470669464.

[9] A. Rogalski, *Infrared and Terahertz Detectors*, 3rd ed. Boca Raton, FL, USA: CRC Press, 2019, doi: 10.1201/b21951.

[10] L. Bürkle and F. Fuchs, "InAs/(GaIn)Sb superlattices: A promising material system for infrared detection," in *Handbook of Infra-Red Detection Technologies*. Amsterdam, The Netherlands: Elsevier, 2002, pp. 159–189, doi: 10.1016/B978-185617388-9/50005-8.

[11] D. Z.-Y. Ting *et al.*, "Type-II superlattice infrared detectors," in *Semiconductors and Semimetals*, vol. 84. Amsterdam, The Netherlands: Elsevier, 2011, pp. 1–57, doi: 10.1016/B978-0-12-381337-4.00001-2.

[12] A. Rogalski, M. Kopytko, and P. Martyniuk, *Antimonide-based Infrared Detectors: A New Perspective*. Bellingham, WA, USA: SPIE, 2018, doi: 10.1117/3.2278814.

[13] A. Rogalski, P. Martyniuk, M. Kopytko, P. Madejczyk, and S. Krishna, "InAsSb-based infrared photodetectors: Thirty years later on," *Sensors*, vol. 20, no. 24, p. 7047, Dec. 2020, doi: 10.3390/s20247047.

[14] D. Z. Ting *et al.*, "InAs/InAsSb type-II strained-layer superlattice infrared photodetectors," *Micromachines*, vol. 11, no. 11, p. 958, Oct. 2020, doi: 10.3390/mi11110958.

[15] J. Piotrowski and A. Rogalski, "Comment on 'temperature limits on infrared detectivities of InAs/In$_x$Ga$_{1-x}$Sb superlattices and bulk Hg$_{1-x}$Cd$_x$Te" [J. Appl. Phys.74, 4774 (1993)]," *J. Appl. Phys.*, vol. 80, no. 4, pp. 2542–2544, Aug. 1996, doi: 10.1063/1.363043.

[16] M. Kopytko and A. Rogalski, "Figure of merit for infrared detector materials," *Infr. Phys. Technol.*, vol. 122, May 2022, Art. no. 104063, doi: 10.1016/j.infrared.2022.104063.

[17] J. Chu, B. Li, K. Liu, and D. Tang, "Empirical rule of intrinsic absorption spectroscopy in Hg$_{1-x}$Cd$_x$Te," *J. Appl. Phys.*, vol. 75, no. 2, pp. 1234–1235, Jan. 1994, doi: 10.1063/1.356464.

[18] D. R. Rhiger, "Performance comparison of long-wavelength infrared type II superlattice devices with HgCdTe," *J. Electron. Mater.*, vol. 40, no. 8, pp. 1815–1822, Aug. 2011, doi: 10.1007/s11664-011-1653-6.

[19] D. Z.-Y. Ting *et al.*, "Superlattice and quantum dot unipolar barrier infrared detectors," *J. Eleactron. Mater.*, vol. 42, no. 11, pp. 3071–3079, Nov. 2013, doi: 10.1007/s11664-013-2641-9.

[20] D. Z. Ting *et al.*, "Mid-wavelength high operating temperature barrier infrared detector and focal plane array," *Appl. Phys. Lett.*, vol. 113, no. 2, Jul. 2018, Art. no. 021101, doi: 10.1063/1.5033338.

[21] A. Soibel *et al.*, "Mid-wavelength infrared InAsSb/InAs nBn detectors and FPAs with very low dark current density," *Appl. Phys. Lett.*, vol. 114, no. 16, Apr. 2019, Art. no. 161103, doi: 10.1063/1.5092342.

[22] D. Z. Ting *et al.*, "Advances in III–V semiconductor infrared absorbers and detectors," *Infr. Phys. Technol.*, vol. 97, pp. 210–216, Mar. 2019, doi: 10.1016/j.infrared.2018.12.034.

[23] Y. H. Kim *et al.*, "HOT InAs/InAsSb nBn detector development for SWaP detector," *Proc. SPIE*, vol. 11741, Apr. 2021, Art. no. 117410Y, doi: 10.1117/12.2587857.

[24] L. Höglund *et al.*, "Manufacturability of type-II InAs/GaSb superlattice detectors for infrared imaging," *Infr. Phys. Techn.*, vol. 84, pp. 28–32, Aug. 2017, doi: 10.106/j.infrared.2017.03.002.

[25] Q. Durlin *et al.*, "InAs/InAsSb superlattice structure tailored for detection of the full midwave infrared spectral domain," *Proc. SPIE*, vol. 10111, Jan. 2017, Art. no. 1011112, doi: 10.1117/12.2250908.

[26] B.-M. Nguyen, G. Chen, A. M. Hoang, S. Abdollahi Pour, S. Bogdanov, and M. Razeghi, "Effect of contact doping in superlattice-based minority carrier unipolar detectors," *Appl. Phys. Lett.*, vol. 99, no. 3, Jul. 2011, Art. no. 033501, doi: 10.1063/1.3613927.

[27] D. Wu, J. Li, A. Dehzangi, and M. Razeghi, "Mid-wavelength infrared high operating temperature pBn photodetectors based on type-II InAs/InAsSb superlattice," *AIP Adv.*, vol. 10, no. 2, Feb. 2020, Art. no. 025018, doi: 10.1063/1.5136501.

[28] A. Soibel *et al.*, "InAs/GaSb superlattice based long-wavelength infrared detectors: Growth, processing, and characterization," *Infr. Phys. Technol.*, vol. 54, no. 3, pp. 247–251, May 2011, doi: 10.1016/j.infrared.2010.12.023.

[29] J. Nguyen, D. Z. Ting, C. J. Hill, A. Soibel, S. A. Keo, and S. D. Gunapala, "Dark current analysis of InAs/GaSb superlattices at low temperatures," *Infr. Phys. Technol.*, vol. 52, no. 6, pp. 317–321, Nov. 2009, doi: 10.1016/j.infrared.2009.05.022.

[30] D. Z.-Y. Ting *et al.*, "A high-performance long wavelength superlattice complementary barrier infrared detector," *Appl. Phys. Lett.*, vol. 95, no. 2, Jul. 2009, Art. no. 023508, doi: 10.1063/1.3177333.

[31] D. Z.-Y. Ting *et al.*, "Antimonide superlattice complementary barrier infrared detector (CBIRD)," *Infr. Phys. Technol.*, vol. 54, no. 3, pp. 267–272, May 2011, doi: 10.1016/j.infrared.2010.12.027.

[32] D. Z. Ting *et al.*, "Long wavelength InAs/InAsSb superlattice barrier infrared detectors with p-type absorber quantum efficiency enhancement," *Appl. Phys. Lett.*, vol. 118, no. 13, Mar. 2021, Art. no. 133503, doi: 10.1063/5.0047937.

[33] C. L. Canedy *et al.*, "Antimonide type-II 'W' photodiodes with long-wave infrared R 0 A comparable to HgCdTe," *J. Electron. Mater.*, vol. 36, no. 8, pp. 852–856, Aug. 2007, doi: 10.1007/s11664-007-0109-5.

[34] C. Canedy *et al.*, "Controlling dark current in type-II superlattice photodiodes," *Infr. Phys. Technol.*, vol. 52, no. 6, pp. 326–334, Nov. 2009, doi: 10.1016/j.infrared.2009.09.004.

[35] P. C. Klipstein *et al.*, "Type II superlattice technology for LWIR detectors," *Proc. SPIE*, vol. 9819, May 2016, Art. no. 98190T, doi: 10.1117/12.2222776.

[36] D. R. Rhiger *et al.*, "Progress with type-II superlattice IR detector arrays," *Proc. SPIE*, vol. 6542, Apr. 2007, Art. no. 654202, doi: 10.1117/12.716101.

[37] D. R. Rhiger, R. E. Kvaas, S. F. Harris, and C. J. Hill, "Characterization of LWIR diodes on InAs/GaSb type-II superlattice material," *Infr. Phys. Technol.*, vol. 52, no. 6, pp. 304–309, Nov. 2009, doi: 10.1016/j.infrared.2009.05.009.

[38] D. R. Rhiger, R. E. Kvaas, S. F. Harris, B. P. Kolasa, C. J. Hill, and D. Z. Ting, "Characterization of barrier effects in superlattice LWIR detectors," *Proc. SPIE*, vol. 7660, Apr. 2010, Art. no. 76601N, doi: 10.1117/12.850531.

[39] A. Khoshakhlagh *et al.*, "Long-wave InAs/GaSb superlattice detectors based on nBn and pin designs," *IEEE J. Quantum Electron.*, vol. 46, no. 6, pp. 959–964, Jun. 2010, doi: 10.1109/JQE.2010.2041635.

[40] E. A. DeCuir *et al.*, "Long-wave type-II superlattice detectors with unipolar electron and hole barriers," *Opt. Eng.*, vol. 51, no. 12, Dec. 2012, Art. no. 124001, doi: 10.1117/1.OE.51.12.124001.

[41] H. S. Kim *et al.*, "Long-wave infrared nBn photodetectors based on InAs/InAsSb type-II superlattices," *Appl. Phys. Lett.*, vol. 101, no. 16, Oct. 2012, Art. no. 161114, doi: 10.1063/1.4760260.

[42] R. G. Humphreys, "Radiative lifetime in semiconductors for infrared detection," *Infr. Phys.*, vol. 26, no. 6, pp. 337–342, Nov. 1986, doi: 10.1016/0020-0891(86)90054-0.

[43] W. van Roosbroeck and W. Shockley, "Photon-radiative recombination of electrons and holes in germanium," *Phys. Rev.*, vol. 94, no. 6, pp. 1558–1560, Jun. 1954, doi: 10.1103/PhysRev.94.1558.

[44] B. V. Olson *et al.*, "Intensity- and temperature-dependent carrier recombination in InAs/$InAs_{1-x}Sb_x$ type-II superlattices," *Phys. Rev. A, Gen. Phys.*, vol. 3, no. 4, Apr. 2015, Art. no. 044010, doi: 10.1103/PhysRevApplied.3.044010.

[45] P. T. Landsberg, *Recombination Semiconductors*. Cambridge, U.K.: Cambridge Univ. Press, 1992, doi: 10.1017/CBO9780511470769.

[46] J. R. Meyer *et al.*, "Auger coefficients in type-II InAs/$Ga_{1-x}In_xSb$ quantum wells," *Appl. Phys. Lett.*, vol. 73, no. 20, pp. 2857–2859, Nov. 1998, doi: 10.1063/1.122609.

[47] R. N. Hall, "Electron-hole recombination in germanium," *Phys. Rev.*, vol. 87, no. 2, p. 387, 1952, doi: 10.1103/PhysRev.87.387.

[48] W. Schockley and W. T. Read, "Statistics of the recombinations of holes and electrons," *Phys. Rev.*, vol. 87, no. 5, pp. 835–842, Jun. 1952, doi: 10.1103/PhysRev.87.835.

[49] S. Maimon and G. W. Wicks, "nBn detector, an infrared detector with reduced dark current and higher operating temperature," *Appl. Phys. Lett.*, vol. 89, no. 15, Oct. 2006, Art. no. 151109, doi: 10.1063/1.2360235.

[50] G. R. Savich, J. R. Pedrazzani, D. E. Sidor, S. Maimon, and G. W. Wicks, "Dark current filtering in unipolar barrier infrared detectors," *Appl. Phys. Lett.*, vol. 99, no. 12, Sep. 2011, Art. no. 121112, doi: 10.1063/1.3643515.

[51] G. L. Hansen, J. L. Schmit, and T. N. Casselman, "Energy gap versus alloy composition and temperature in $Hg_{1-x}Cd_xTe$," *J. Appl. Phys.*, vol. 53, no. 10, pp. 7099–7101, Oct. 1982, doi: 10.1063/1.330018.

[52] P. Knowles *et al.*, "Status of IR detectors for high operating temperature produced by MOVPE growth of MCT on GaAs substrates," *Proc. SPIE*, vol. 8541, Nov. 2012, p. 854108, doi: 10.1117/12.971431.

[53] P. Martyniuk and A. Rogalski, "Performance comparison of barrier detectors and HgCdTe photodiodes," *Opt. Eng.*, vol. 53, no. 10, Nov. 2014, Art. no. 106105, doi: 10.1117/1.OE.53.10.106105.

[54] P. C. Klipstein *et al.*, "Low SWaP MWIR detector based on XBn focal plane array," *Proc. SPIE*, vol. 8704, Jun. 2013, Art. no. 87041S, doi: 10.1117/12.2015747.

[55] C. T. Elliott, N. T. Gordon, and A. M. White, "Towards background-limited, room-temperature, infrared photon detectors in the 3–13 μm wavelength range," *Appl. Phys. Lett.*, vol. 74, no. 19, pp. 2881–2883, May 1999, doi: 10.1063/1.124045.

[56] P. Jerram and J. Beletic, "Teledyne's high performance infrared detectors for space missions," in *Proc. Int. Conf. Space Opt. (ICSO)*, Jul. 2019, p. 120, doi: 10.1117/12.2536040.

[57] A. Rogalski, P. Martyniuk, M. Kopytko, and W. Hu, "Trends in performance limits of the HOT infrared photodetectors," *Appl. Sci.*, vol. 11, no. 2, p. 501, Jan. 2021, doi: 10.3390/app11020501.

[58] G. L. Hansen and J. L. Schmit, "Calculation of intrinsic carrier concentration in $Hg_{1-x}Cd_xTe$," *J. Appl. Phys.*, vol. 54, no. 3, pp. 1639–1640, Mar. 1983, doi: 10.1063/1.332153.

[59] Y. P. Varshni, "Temperature dependence of the energy gap in semiconductors," *Physica*, vol. 34, no. 1, pp. 149–154, Jan. 1967, doi: 10.1016/0031-8914(67)90062-6.

[60] D. Z. Ting, A. Soibel, and S. D. Gunapala, "Type-II superlattice hole effective masses," *Infr. Phys. Tech.*, vol. 84, pp. 102–106, Aug. 2017, doi: 10.1016/j.infrared.2016.10.014.

[61] D. Z. Ting *et al.*, "Advances in III–V semiconductor infrared absorbers and detectors," *Infr. Phys. Technol.*, vol. 97, pp. 210–216, Mar. 2019, doi: 10.1016/j.infrared.2018.12.034.

[62] D. Z.-Y. Ting, A. Soibel, L. Höglund, and S. D. Gunapala, "Theoretical aspects of minority carrier extraction in unipolar barrier infrared detectors," *J. Electron. Mater.*, vol. 44, no. 9, pp. 3036–3043, Sep. 2015, doi: 10.1007/s11664-015-3756-y.

[63] A. Tibaldi, J. A. G. Montoya, M. Vallone, M. Goano, E. Bellotti, and F. Bertazzi, "Modeling infrared superlattice photodetectors: From nonequilibrium Green's functions to quantum-corrected drift diffusion," *Phys. Rev. A, Gen. Phys.*, vol. 16, no. 4, Oct. 2021, Art. no. 044024, doi: 10.1103/PhysRevApplied.16.044024.